Enhancing quantum utility: Simulating large-scale quantum spin chains on superconducting quantum computers

Talal Ahmed Chowdhury [1,2,*] Kwangmin Yu [3,†] Mahmud Ashraf Shamim [4] M. L. Kabir [5] and Raza Sabbir Sufian [6,7]

[1]*Department of Physics and Astronomy, University of Kansas, Lawrence, Kansas 66045, USA*
[2]*Department of Physics, University of Dhaka, P.O. Box 1000 Dhaka, Bangladesh*
[3]*Computational Science Initiative, Brookhaven National Laboratory, Upton, New York 11973, USA*
[4]*Department of Physics and Astronomy, University of Alabama, Tuscaloosa, 35487 Alabama, USA*
[5]*Collider-Accelerator Department, Brookhaven National Laboratory, Upton, New York 11973, USA*
[6]*RIKEN-BNL Research Center, Brookhaven National Laboratory, Upton, New York 11973, USA*
[7]*Physics Department, Brookhaven National Laboratory, Upton, New York 11973, USA*

(Received 18 March 2024; accepted 26 June 2024; published 25 July 2024)

We present the quantum simulation of the frustrated quantum spin-$\frac{1}{2}$ antiferromagnetic Heisenberg spin chain with competing nearest-neighbor (J_1) and next-nearest-neighbor (J_2) exchange interactions in the real superconducting quantum computer with qubits ranging up to 100. In particular, we implement the Hamiltonian with the next-nearest neighbor exchange interaction in conjunction with the nearest-neighbor interaction on IBM's superconducting quantum computer and carry out the time evolution of the spin chain by employing the first-order Trotterization. Furthermore, our implementation of the second-order Trotterization for the isotropic Heisenberg spin chain, involving only nearest-neighbor exchange interaction, enables precise measurement of the expectation values of staggered magnetization observable across a range of up to 100 qubits. Notably, in both cases, our approach results in a constant circuit depth in each Trotter step, independent of the number of qubits. Our demonstration of the accurate measurement of expectation values for the large-scale quantum system using superconducting quantum computers designates the quantum utility of these devices for investigating various properties of many-body quantum systems. This will be a stepping stone to achieving the quantum advantage over classical ones in simulating quantum systems before the fault tolerance quantum era.

DOI: 10.1103/PhysRevResearch.6.033107

I. INTRODUCTION

The landscape of quantum computing has experienced significant evolution, especially with the emergence of noisy intermediate-scale quantum (NISQ) computers [1,2] and beyond at scale such as IBM Quantum processors. Despite their inherent noise and limitations, these platforms have opened up new avenues for delving into fundamental physics. Quantum simulation [3–5] of seemingly complex many-body quantum systems using near-term, noisy quantum computers presents an intriguing possibility. While the algorithm for quantum simulation using quantum computers was initially outlined for many-body Hamiltonians in Ref. [6] and subsequently refined in works such as [7–14], its actual implementation on a quantum computer necessitates comprehensive quantum error correction.

Using near-term, noisy quantum computers to simulate fundamental physics presents significant challenges including error rates that affect computation accuracy, constraints on qubit numbers limiting the complexity of simulated systems, and difficulty in maintaining qubit stability over extended periods. Nevertheless, ongoing advancements in error-mitigation techniques and algorithms [15–22] for noisy quantum devices are enhancing their capability to perform detailed and accurate simulations of fundamental physics. These successes showed the utility of noisy quantum computers before the advent of fault-tolerance [22]. Despite these advancements, an important question remains: are currently available quantum computers capable of simulating large quantum systems and extracting precise values for observables on more realistic problems? This question warrants further investigation to assess the practical limitations and potential of current quantum technology in the realm of large-scale quantum simulations. Recently, Kim *et al*. [22] successfully performed time evolution simulation of the Ising model on IBM quantum computers at a scale beyond exact classical methods with accuracy competitive with tensor network methods. However, it remains an open problem to achieve such quantum utility for a broader range of practical problems.

In this study, we expand the utility of noisy quantum computers to more general and complicated cases of time evolution driven by Hamiltonians at large-scale noisy superconducting quantum computers. We focus on the simulation for the time evolution of quantum spin-$\frac{1}{2}$ antiferromagnetic

*Contact author: talal@ku.edu
†Contact author: kyu@bnl.gov

Heisenberg model with frustration and assess their ability to accurately capture the intricate spin dynamics of the model. The frustrated spin-$\frac{1}{2}$ antiferromagnetic model serves as a paradigmatic representation of a quantum many-body system characterized by competing interactions among its constituents. In a magnetically frustrated system, the ground state becomes degenerate due to the inherent ambiguity of the spin configurations not being able to satisfy all of the antiferromagnetic interactions simultaneously. Consequently, the ground state of the frustrated systems becomes highly entangled, leading to exotic phases of quantum matters such as quantum spin liquids (QSLs) [23–25].

In particular, we consider the spin-$\frac{1}{2}$ antiferromagnetic spin chain with competing nearest-neighbor (J_1) and next-nearest-neighbor (J_2) exchange interactions [26,27] in the real superconducting quantum computer with qubits ranging up to 100. The antiferromagnetic quantum spin chain has a rich ground-state quantum phase diagram [28–32]. Apart from its rich quantum phase structure, interestingly, the antiferromagnetic spin chain model can be related to the Schwinger model [33–36], a toy model in $(1+1)$ dimensions [$(1+1)$D] that captures the features of a strongly coupled sector of quantum chromodynamics (QCD). To simulate the time evolution of the quantum spin-$\frac{1}{2}$ antiferromagnetic Heisenberg spin chain with competing nearest-neighbor and next-nearest-neighbor exchange interactions on noisy superconducting quantum computers, we developed a new Trotterization [37–39] circuit design. The main challenge of the circuit design is originated by the limited connectivity of superconducting quantum computers. Since the model has the interaction between the next-nearest-neighbor in addition to the nearest neighbor, the limited connectivity of the system is a huge barrier for efficient Trotterization while the nearest-neighbor interaction can be efficiently implemented on linear qubit connectivity. Our new circuit design for the model is suitable for linear qubit connectivity (circular connectivity for a periodic boundary condition). Also, the design has a constant circuit depth with respect to the system size (the number of qubits) so that this implementation is scalable. This circuit design is described in detail in Sec. III B.

Moreover, a special case ($J_2 = 0$) of the model is the Heisenberg isotropic spin chain model. In this case, we propose a new second-order Trotterization implementation. In general, a second-order Trotterization has twice the longer circuit depth than the corresponding first-order Trotterization. However, we achieve the second-order Trotterization by only an additional constant circuit depth than the circuit depth of the first-order Trotterization. Since we have a trade-off between numerical noise and quantum device noise when we increase the order of Trotterization, implementing the second-order Trotterization with only constant circuit depth increase from the first-order Trotterization is a great benefit. The implementation detail is described in Sec. III A.

Subsequently, we validate our new circuit designs with 20, 96, and 100 qubit systems on the IBM quantum processors of 127 qubits and 133 qubits. To cope with the quantum errors and noises, we apply several quantum error mitigation methods to our new circuit designs (Refer to Sec. IV B). We successfully simulate the time evolution with 3888 and 3978 CX gates using open and periodic boundary conditions, respectively, that are presented in Sec. V. Finally, we conclude in Sec. VI.

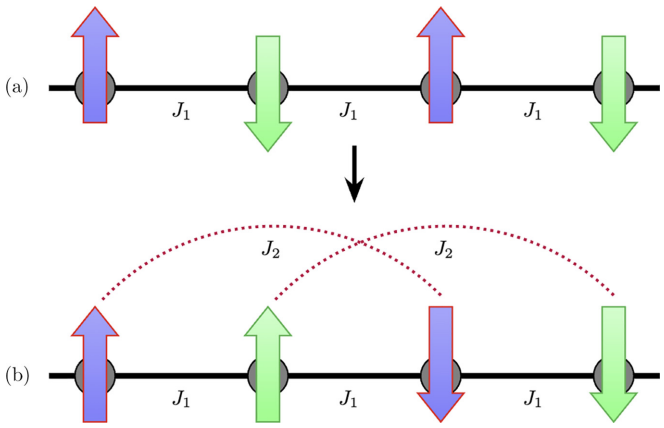

FIG. 1. (a) In the absence of frustration, the nearest-neighbor interaction prefers the antiferromagnetic or the Néel ordering. (b) In contrast, the onset of next-nearest-neighbor interaction J_2 makes the system frustrated as it favors the antiparallel alignment of the next-nearest-neighboring spins, leading to a parallel combination between neighboring spin pairs.

II. FRUSTRATED SPIN-$\frac{1}{2}$ ANTIFERROMAGNETIC SPIN CHAIN MODEL

The frustrated spin-$\frac{1}{2}$ antiferromagnetic Heisenberg spin chain is described by the following Hamiltonian:

$$H = J_1 \sum_{i=1}^{N} \left(S_i^x S_{i+1}^x + S_i^y S_{i+1}^y + \Delta S_i^z S_{i+1}^z\right) + J_2 \sum_{i=1}^{N} \left(S_i^x S_{i+2}^x + S_i^y S_{i+2}^y + S_i^z S_{i+2}^z\right), \tag{1}$$

where the antiferromagnetic nearest-neighbor (NN) coupling $J_1 > 0$, next-nearest-neighbor (NNN) coupling $J_2 \geqslant 0$ and the exchange-anisotropy parameter $\Delta \geqslant 0$ control the parameter space of the Hamiltonian. Besides, the spin operators, $S^i = \frac{1}{2}\sigma^i$ obey the SU(2) algebra,

$$\left[S_i^\alpha, S_j^\beta\right] = i\delta_{ij}\epsilon^{\alpha\beta\gamma} S_i^\gamma, \tag{2}$$

where $\alpha, \beta, \gamma = x, y, z$ and $i, j = 1, \ldots, N$. Our analysis considers open boundary conditions (OBC) and periodic boundary conditions (PBC). The PBC is imposed by setting $S_{i+N}^\alpha = S_i^\alpha$. Besides, we take the total number of spin sites on the chain as even $N = 4n$, where n takes on positive integers. Additionally, this Hamiltonian is referred to spin-$\frac{1}{2}$ $J_1 - J_2$ XXZ Hamiltonian in many instances. From Fig. 1, we can see that when the next-nearest-neighbor interaction J_2 is set to zero, the spin alignment, for example along the z axis, follows the antiferromagnetic ordering but the onset of J_2 introduces a competing interaction which would disrupt the initial antiferromagnetic ordering for large enough J_2 value. Hence, the spin chain becomes frustrated.

The couplings (J_1, J_2, Δ) of the Hamiltonian would result in a rich ground-state phase diagram of the frustrated quantum spin-$\frac{1}{2}$ antiferromagnetic spin chain. In the subsequent

analysis, we focus on two important Hamiltonians for particular parameter values, as detailed below.

Isotropic Heisenberg Hamiltonian. The isotropic Heisenberg Hamiltonian, also known H_{iso}, is characterized by the parameters, $J_1 > 0$, $J_2 = 0$, and $\Delta = 1$. Unlike the general case of $\Delta \neq 1$, it has a full global SU(2) symmetry.

Dimer Hamiltonian. The dimer Hamiltonian corresponding to the Majumdar-Ghosh (MG) point, denoted here as H_{dimer}, is characterized by $J_1 > 0$, $J_2 = \frac{J_1}{2}$, $\Delta = 1$ [40,41]. It also enjoys the full SU(2) symmetry. The crucial feature of this Hamiltonian is that its ground state manifests as a doubly degenerate valence bond solid (VBS) phase where the pairs of neighboring spins on the chain form spin-singlets, referred to as dimer states.

A. Time evolution of the quantum system

In this work, we focus on the time evolution of the spin chain under the Hamiltonians, H_{iso} and H_{dimer}. As our focus is to study the accuracy of the measurement of observables associated with the spin chain at the superconducting quantum computers, we focus on the temporal variation of the expectation value of the staggered magnetization that characterizes the antiferromagnetic ordering in the spin chain. The staggered magnetization observable $\hat{O}_{M_{st}}$ is defined as follows:

$$\hat{O}_{M_{st}} = \frac{1}{N}\sum_{i=1}^{N}(-1)^i S_i^z. \tag{3}$$

One can choose a specific spin configuration of the quantum spin chain and calculate the expectation value of the staggered magnetization observable to characterize the spin states' antiferromagnetic ordering. There exist myriad options for selecting such spin states. However, for simplicity and clarity, we opt for the Néel state that encapsulates some of the fundamental features of the antiferromagnetic spin chain. It is defined as

$$|\psi_{\text{Neel}}\rangle = |\uparrow\downarrow\uparrow\downarrow\cdots\cdots\uparrow\downarrow\uparrow\downarrow\rangle, \tag{4}$$

where each $|\uparrow\rangle$ or $|\downarrow\rangle$ represent the spin projection of spin-1/2 particle at the ith site along the z axis in spin space.

Consequently, we determine the time evolution of the expectation value of staggered magnetization observable for the Néel state under the Hamiltonian H_{iso} and H_{dimer} in IBM's superconducting quantum computers and corroborated the results with state-of-the-art classical numerical tools.

III. IMPLEMENTATION OF TIME EVOLUTION UNDER THE SPIN CHAIN HAMILTONIAN

Starting from this section, we use 0 as the first index instead of 1 to keep consistency with IBM Qiskit's qubit index convention. Hence, the index varies from 0 to $N-1$ instead of from 1 to N. Also, we assume N is even. Equation (1) is reformulated by the Pauli operators, $\sigma_j^x, \sigma_j^y, \sigma_j^z$ as follows:

$$H = \sum_{j=0}^{N-1}\left(J_x\sigma_j^x\sigma_{j+1}^x + J_y\sigma_j^y\sigma_{j+1}^y + J_z\sigma_j^z\sigma_{j+1}^z\right) + \frac{J_2}{4}\sum_{j=0}^{N-1}\left(\sigma_j^x\sigma_{j+2}^x + \sigma_j^y\sigma_{j+2}^y + \sigma_j^z\sigma_{j+2}^z\right), \tag{5}$$

where $J_z = \Delta J_1/4$ and $J_x = J_y = J_1/4$.

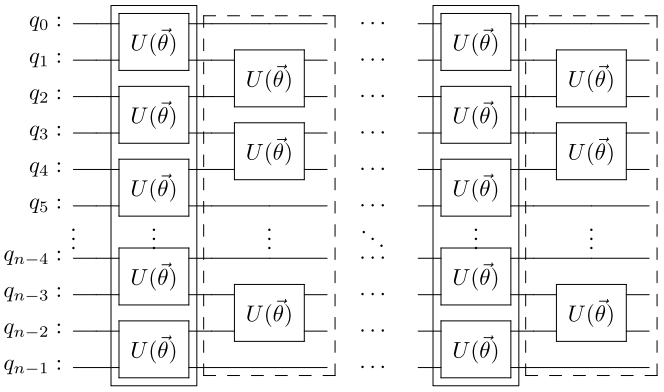

FIG. 2. The first-order Trotterization of the Hamiltonian H_{iso} with open boundary condition. The layers surrounded by the straight lines are the even layers and the layers surrounded by the dotted lines are the odd layers. For a periodic boundary condition, the odd layers have the two-qubit gates, $U(\vec{\theta})$, between q_{n-1} and q_0. One Trotter step is composed of the even layer and the odd layer.

A. The second-order Trotterization for isotropic Heisenberg Hamiltonian

In this section, we address a specific case of the Hamiltonian [Eq. (5)], which has $J_2 = 0$. We have a basic building block for the time evolution as follows:

$$U_j(\vec{\theta}) = \exp\left[-i\left(\frac{\theta_x}{2}\sigma_j^x\sigma_{j+1}^x + \frac{\theta_y}{2}\sigma_j^y\sigma_{j+1}^y + \frac{\theta_z}{2}\sigma_j^z\sigma_{j+1}^z\right)\right], \tag{6}$$

where $\vec{\theta} = (\theta_x, \theta_y, \theta_z) = (2J_x\Delta t,\ \ 2J_y\Delta t,\ \ 2J_z\Delta t)$ with the Trotter step size Δt. By the Trotter approximation, we can arrange the $U_i(\vec{\theta})$ operators in staggered placement [42,43] as shown in Fig. 2. Hence, one Trotter step is formulated as follows:

$$U(\vec{\theta}) = \left(\prod_{j=0}^{N/2-1} U_{2j}(\vec{\theta})\right)\left(\prod_{j=0}^{N/2-1} U_{2j+1}(\vec{\theta})\right).$$

We define the even layer $U_e(\vec{\theta})$ and the odd layer $U_o(\vec{\theta})$ as follows:

$$U_e(\vec{\theta}) = \left(\prod_{j=0}^{N/2-1} U_{2j}(\vec{\theta})\right), \quad U_o(\vec{\theta}) = \left(\prod_{j=0}^{N/2-1} U_{2j+1}(\vec{\theta})\right),$$

respectively. The even layers and the odd layers are highlighted in straight lines and dotted lines, respectively, in Fig. 2. The first-order Trotterization (Fig. 2) needs $2M$ layers when we have M Trotter steps.

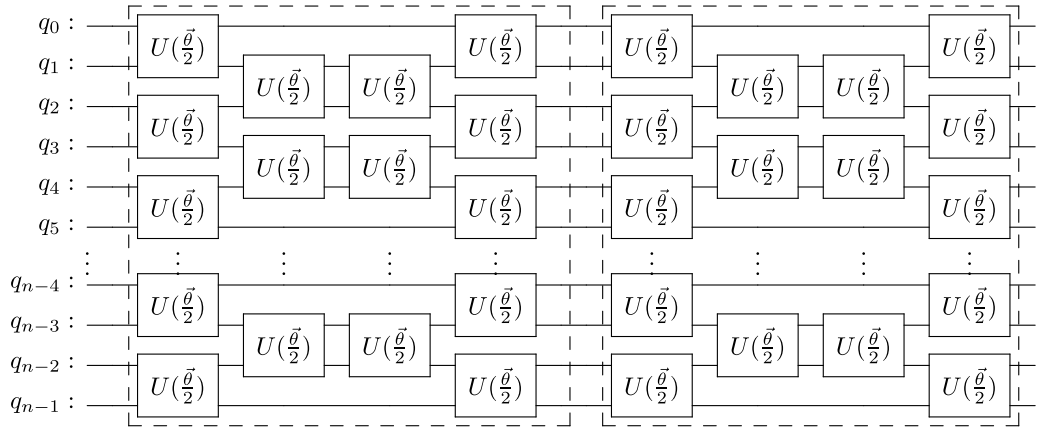

FIG. 3. The second-order Trotterization of the Hamiltonian H_{iso} with open boundary condition with two Trotter steps. The dotted parts are one Trotter step of the second-order. The one step of the second-order Trotterization is composed of an even layer, an odd layer, an odd layer, and an even layer in order. For a periodic boundary condition, the odd layers have the two-qubit gates, $U(\frac{\vec{\theta}}{2})$, between q_{n-1} and q_0.

The second-order Trotterization is described in Fig. 3. Even though the accuracy of the second-order Trotterization increases, the circuit depth increases double in general. However, we can compress the circuits of the second-order Trotterization for the Heisenberg XXX spin chain Hamiltonian. It is trivial since we have the following equality:

$$U_e(\vec{\theta}_1)U_e(\vec{\theta}_2) = U_e(\vec{\theta}_1 + \vec{\theta}_2) \text{ and } U_o(\vec{\theta}_1)U_o(\vec{\theta}_2) = U_o(\vec{\theta}_1 + \vec{\theta}_2).$$

Hence, we can merge the adjacent odd layers, and the last even layer can be merged with the first even layer of the next Trotter step. Figure 4 shows the merged circuit diagram of the second-order Trotterization in Fig. 3. The merged second-order Trotterization depicted in Fig. 4 shows that the implementation needs only $2M + 1$ layers when we have M Trotter steps. Note that the first-order Trotterization (cf. Fig. 2) has $2M$ layers with M Trotter steps. We achieve the second-order Trotterization by adding one even layer at the end of the first-order Trotterization and adjusting the angle parameters ($\vec{\theta}$). Considering the trade-off between the Trotterization error and the quantum noise when we use a higher-order Trotterization, it is a great benefit to achieve the second-order Trotterization with only constant circuit depth.

B. The first-order Trotterization for the dimer Hamiltonian

The dimer Hamiltonian H_{dimer} has additional terms in addition to the Heisenberg XXX spin chain Hamiltonian H_{iso} as shown in Eq. (1). The additional terms have coefficient J_2. The J_2 terms have interaction with the next nearest-neighbor sites. Hence, the dimer Hamiltonian has the interaction with the nearest neighbor and the next-nearest-neighbor sites. This is the main challenge to make a quantum circuit for the time evolution of the Hamiltonian on quantum computers having limited connectivity between qubits such as in superconducting quantum computers.

In this section, we describe our new quantum circuit design for the dimer Hamiltonian on the quantum devices having only connection between nearest-neighbor qubits. That is, all qubits have two connections except the first and the last qubits (a path graph) on open boundary conditions. In periodic boundary conditions, the first and the last qubits are connected (a circle graph). Figure 5 shows one Trotter step of the first-order Trotterization for the dimer Hamiltonian. In the figure, the box surrounded by the straight line is the isotropic Heisenberg Hamiltonian part (cf. Fig. 2). The dotted box part in Fig. 5 represents our new circuit design for the J_2 terms.

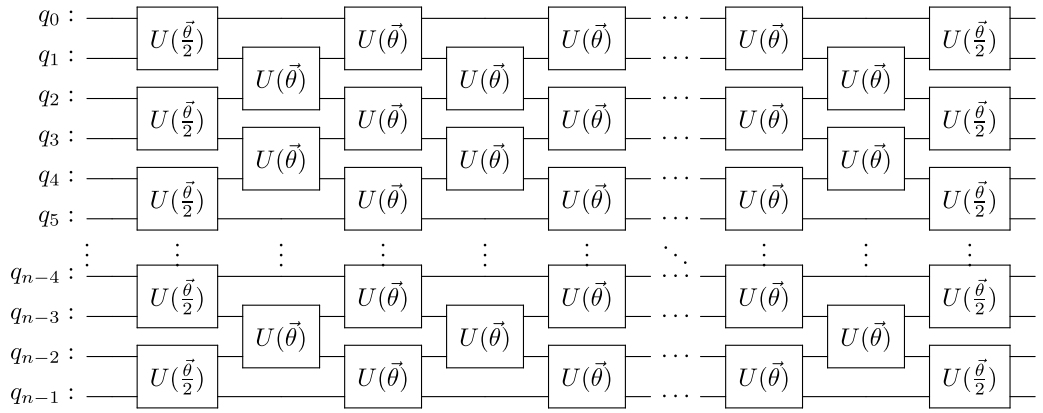

FIG. 4. The optimized second-order Trotterization of the Hamiltonian H_{iso} with open boundary condition with two Trotter steps. For a periodic boundary condition, the odd layers have the two-qubit gates, $U(\vec{\theta})$, between q_{n-1} and q_0. The circuit diagram in Fig. 3 is optimized by merging adjacent even layers and odd layers, respectively.

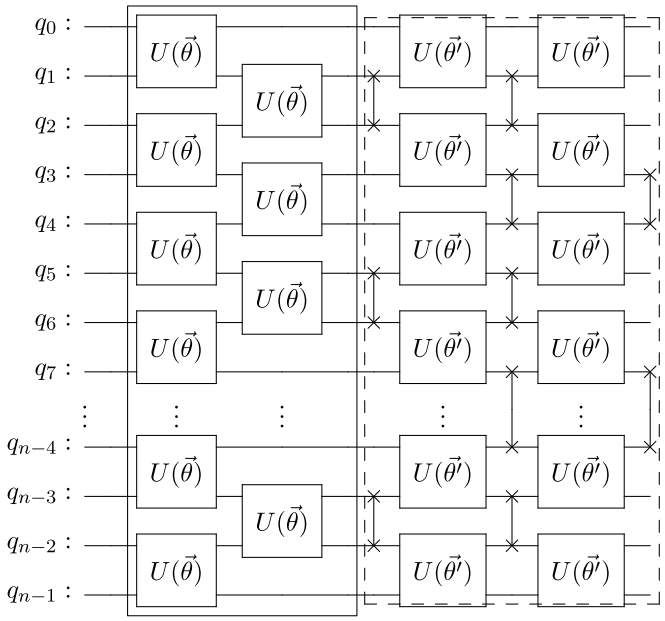

FIG. 5. One Trotter step implementation for the Hamiltonian H_{dimer}. Here, $\theta = 2J_1\delta t$ and $\theta' = 2J_2\delta t = J_1\delta t$ (as for dimer case, $J_2 = J_1/2$). For a periodic boundary condition, the odd layers in the straight line box have the two-qubit gates, $U(\vec{\theta})$, between q_{n-1} and q_0 and the SWAP gate between q_{n-1} and q_0 in the second and the third SWAP gate layers in the dotted line box.

In this circuit design, we assume that the n is a multiple of four. In the numbering notation, the upper bar of a number represents a modulo number of four. For example, $\bar{k}$ means k mod four. In addition, SWAP(i, j) represents the SWAP gate between q_i and q_j. The first step is placing SWAP$(\bar{1}, \bar{2})$. This is depicted in the first SWAP layer in the dotted box in Fig. 5. The second is placing the even layer on the whole qubits. The first SWAP gate layer and the following even layers process the J_2 terms between $\bar{0}$ and $\bar{2}$, and $\bar{1}$ and $\bar{3}$, respectively. The third is placing SWAP$(\bar{1}, \bar{2})$, and SWAP$(\bar{3}, \bar{0})$ of the neighbor. If it is under PBC, SWAP$(n-1, 0)$ is added. SWAP$(\bar{1}, \bar{2})$ is reversing the first step, SWAP$(\bar{1}, \bar{2})$. The fourth is placing the even layer on the whole qubits. SWAP$(\bar{3}, \bar{0})$ of the neighbor and the following even layers process the J_2 terms between $\bar{2}$ and $\bar{0}$, and $\bar{3}$ and $\bar{1}$, respectively. Finally, SWAP$(\bar{3}, \bar{0})$ of neighbor are placed. If it is under PBC, SWAP$(n-1, 0)$ is added. The final process is reversing the SWAP$(\bar{3}, \bar{0})$ of the neighbor in the third process. The whole process of the circuit construction is summarized in Table I.

Finally, we remark on the second-order Trotterization of the dimer Hamiltonian. In contrast with the isotropic Heisenberg Hamiltonian in Sec. III A, the second-order Trotterization of the dimer Hamiltonian does not have a significant benefit. The first-order Trotterization of the dimer Hamiltonian has seven layers including the three SWAP gate layers for one Trotter step as shown in Fig. 5 while the second-order Trotterization needs twelve layers. Even though the Trotterization error (numerical error) will decrease when we adopt the second-order Trotterization instead of the first-order Trotterization, the quantum device error by the longer circuit depth will increase and we anticipate the device error would be more dominant than the gain of the decrease of the numerical error. Hence, we do not adopt the second-order Trotterization in our experiments for the dimer Hamiltonian.

TABLE I. Summary of the circuit construction for the J_2 terms in Fig. 5.

Notation
n is the number of qubits and a multiple of 4.
The numbers represent qubit index from 0 to $n-1$.
$\bar{k}$ represent k modulo 4.
1: Place SWAP gates between $\bar{1}$ and $\bar{2}$.
2: Place the even layer of $\vec{\theta}'$ on the whole qubits.
3: Place SWAP gates between $\bar{1}$ and $\bar{2}$, and between $\bar{3}$ and $\bar{0}$. if PBC, place SWAP gate between $n-1$ and 0.
4: Place the even layer of $\vec{\theta}'$ on the whole qubits.
5: Place SWAP gates between $\bar{3}$ and $\bar{0}$. if PBC, place SWAP gate between $n-1$ and 0.

IV. IMPLEMENTATION FOR EXPERIMENTS

As we discussed in the previous section, the basic building block for the quantum circuit implementation is $U_i(\vec{\theta})$ in Eq. (6) for both the isotropic Heisenberg Hamiltonian H_{iso} and the dimer Hamiltonian H_{dimer}. Hence, the key to a successful simulation on noisy quantum computers lies in the implementation of an efficient quantum circuit, as contemporary noisy quantum computers are susceptible to various quantum noise sources, including quantum gate errors. In this section, we describe our specific circuit implementation of Eq. (6) to execute the time evolution on the IBM quantum computers. Section IV A summarizes the quantum circuit implementation. As described in Sec. III, we need only an efficient implementation of Eq. (6) for the time evolution of the isotropic Heisenberg Hamiltonian (H_{iso}) and the dimer Hamiltonian (H_{dimer}) as well as SWAP gates between the nearest-neighbor qubits. Since our new circuit implementations for H_{iso} and H_{dimer} only use quantum gates working on the nearest-neighbor qubits, these implementations circumvent the limited qubit connection issue of IBM quantum computers. Based on the quantum circuit implementation, various quantum error mitigation methods are applied and the methods are described in Sec. IV B.

A. Quantum circuit implementation

To implement Eq. (6), we start from the Ising coupling gate $R_{Z_iZ_j}(\theta)$ as follows:

$$R_{Z_iZ_j}(\theta) = \exp\left(-i\frac{\theta}{2}\sigma_i^z\sigma_j^z\right) = \begin{pmatrix} e^{-i\frac{\theta}{2}} & 0 & 0 & 0 \\ 0 & e^{i\frac{\theta}{2}} & 0 & 0 \\ 0 & 0 & e^{i\frac{\theta}{2}} & 0 \\ 0 & 0 & 0 & e^{-i\frac{\theta}{2}} \end{pmatrix},$$

which is implemented as `RZZGate` in IBM Qiskit. Since we have Clifford gate identities, we have the induced $R_{X_iX_j}(\theta)$ and $R_{Y_iY_j}(\theta)$ gates as follows:

$R_{XX}(\theta) =$ 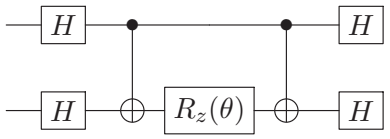

$R_{YY}(\theta) =$ 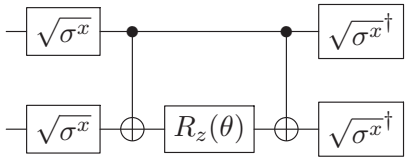

$R_{ZZ}(\theta) =$ 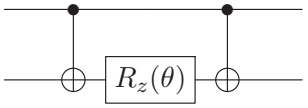

where H is the Hadamard gate,

$$(\sigma^x)^{1/2} = \frac{1}{2}\begin{pmatrix} 1+i & 1-i \\ 1-i & 1+i \end{pmatrix},$$

and

$$R_z(\theta) = \begin{pmatrix} e^{-i\frac{\theta}{2}} & 0 \\ 0 & e^{i\frac{\theta}{2}} \end{pmatrix}.$$

Hence, $U_i(\vec{\theta})$ in Eq. (5) is implemented as follows:

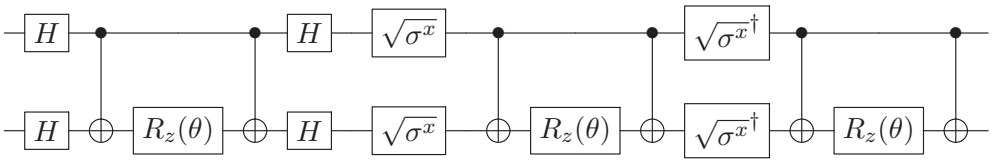

(7)

and this implementation has six `CX` gates and thirteen circuit depths. This circuit is compressed and optimized by circuit identities as follows:

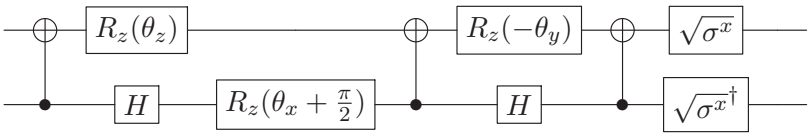

(8)

This circuit has three `CX` gates and seven depths. The induction of the circuit identity is described in detail in Appendix A in Ref. [44]. Since quantum gates have gate errors and two-qubit gates such as `CX` are noisier than single-qubit gates, reducing the number of `CX` gates as well as the circuit depths is essential to reduce the overall noise on the quantum computers. Hence, we adopt the quantum circuit described in Eq. (8) for the implementation of Eq. (6).

B. Quantum error mitigations

The troublesome challenge of running quantum algorithms on contemporary quantum devices, including IBM Quantum processors, is the errors and noise on the quantum devices To cope with the errors and noises, quantum error correction (QEC) was suggested [45,46]. However, QEC has a qubit overhead that is daunting to implement on a large problem on the contemporary quantum processors even though they are optimized [47,48]. On the other hand, quantum error mitigation (QEM) accepts the imperfection of contemporary quantum devices and adopts methods of mitigating or suppressing quantum errors and noises. QEM has a low or no qubit overhead. In recent years, various QEM methods have been developed, and their practicality has been proven in practical problems [20–22,49]. Hence, we apply four QEM methods, zero-noise extrapolation (ZNE), Pauli twirling (PT), dynamical decoupling (DD), and matrix-free measurement mitigation (M3) to cope with the quantum device errors and noises in our experiments. A quantum circuit for one Hamiltonian simulation at a time is extended to three variational

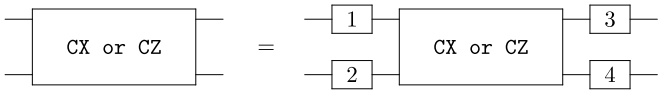

FIG. 6. A circuit diagram for Pauli twirling for CX, CZ, or ECR gates. At positions 1, 2, 3, and 4, Pauli gates, $\{I, \sigma^x, \sigma^y, \sigma^z\}$ are placed.

circuits including itself for the ZNE method and each variational circuit is duplicated to ten copies to apply the PT. Hence, we have 30 circuits for one Hamiltonian simulation at a time. We explain the QEM methods in detail in the following subsections.

1. Zero-noise extrapolation

Zero-noise extrapolation (ZNE) is a quantum error mitigation method that estimates an ideal expectation value (no noise expectation value) from other expectation values at different noise levels by extrapolation methods [16,17,50]. In our experiments, we adopted local unitary gate folding [50] with scaling factors 1, 3, and 5 only on two-qubit gates such as CX (or CZ. Refer to Sec. IV C) gates rather than applying the folding to all gates since the two-qubit gate is more than ten times noisier than single qubit gates.

2. Pauli twirling

Pauli twirling is a method averaging out the off-diagonal coherent errors of the circuits in the Pauli basis, $\{I, \sigma^x, \sigma^y, \sigma^z\}$ [51–53]. In Pauli twirling, a Clifford gate is surrounded by the Pauli gates back and forth which is mathematically identical to the Clifford gate. The efficiency is empirically proved in previous studies [21,22]. Figure 6 shows the Pauli twirling method we applied to this study. First, we searched all the combinations of Pauli gates that are mathematically identical up the global phase with only the Clifford gate (CX or CZ gate depending on the target quantum device in our experiments). This is our Pauli twirling gates set. Since the Pauli gate set has four elements and we have four positions, the search domain is $256(= 4^4)$ cases. The trivial case is placing the identity gate in the position 1, 2, 3, and 4 in Fig. 6. One nontrivial case is putting σ^z, σ^x, σ^z, and σ^x at 1, 2, 3, and 4, respectively. We duplicated 10 copies of the base quantum circuit. After that, we randomly chose a Pauli twirling gate combination out of the prepared Pauli twirling gates set and applied them to the Clifford gate as described in Fig. 6.

3. Dynamical decoupling

Dynamical decoupling (DD) is a quantum error mitigation method that reduces errors caused by spectator qubits. DD is implemented by periodic sequences of instantaneous control pulses that average out the coupling with the system environment to approximately zero [54]. In particular, a set of single qubit operators are interleaved using basis transformation on idle qubits so that environmental contamination from other qubits is decoupled. Consequently, the coherence time of the circuit becomes longer. The efficiency of DD is empirically tested in various environments [21,22,49,55,56]. In this study, we added $(t/4, \sigma^x, t/2, \sigma^x, t/4)$ sequence in every idling period through Qiskit PassManager, where t is the idling time except for the two XGate pulse durations.

4. Measurement error mitigation

The canonical measurement error mitigation methods [57–59] correct the measurement error over N qubits by computing the measurement error probability matrix as follows:

$$\vec{s}_{\text{noisy}} = \mathcal{M}\vec{s}_{\text{ideal}},$$

where $\vec{s}_{\text{noisy}}$ and $\vec{s}_{\text{ideal}}$ are a state vector of noisy probabilities returned by the quantum system, and a state vector of the probabilities in the absence of measurement errors, respectively. Since $\vec{s}_{\text{noisy}}$ and $\vec{s}_{\text{ideal}}$ are state vectors of N qubits, the matrix $\mathcal{M}$ has $2^N \times 2^N$ dimension with entry $A_{i,j}$ is the probability of bit string j being converted to bit string i by the measurement-error process. Although errors across multiple qubits can be accurately approximated by employing no more than $O(N)$ calibration circuits, the method has to compute the inverse of $\mathcal{M}$ in order to estimate the ideal measurement after getting noisy measurement results. This makes the method impractical at large qubit numbers. Instead of the canonical measurement error mitigation methods, a matrix-free measurement mitigation (M3) method has been invented [60]. The method M3 works in a reduced subspace determined by the noisy input bit strings requiring correction. This space often contains significantly fewer unique bit strings compared with the expansive multiqubit Hilbert space, making the resulting set of linear equations notably simpler to resolve. This method is implemented in Python [61]. Since we conducted the experiments with 20, 96, and 100 qubits, it was not possible to use the canonical measurement error mitigation methods. So, We adopted M3 for our measurement error mitigation by using the implementation [61].

C. Circuit implementation for experiments and post processing

In this study, we used two 127-qubit IBM quantum processors, ibm_sherbrooke, ibm_brisbane, and one 133-qubit IBM quantum processor, ibm_torino. The 127-qubit processors are IBM Eagle r3 quantum processors and they have a basis gate set, {ECR, I, RZ, SX, X} where I, RZ, SX, and ECR are the identity, R_z, $(\sigma^x)^{1/2}$, and $\frac{1}{\sqrt{2}}(IX - XY)$, respectively [62–64]. On the other hand, the 133-qubit processors adopt the IBM Heron r1 processor type. This type has the basis gate set {CZ, I, RZ, SX, X}, where CZ is a controlled-Z gate, $I \otimes |0\rangle\langle 0| + Z \otimes |0\rangle\langle 0|$ or $Z \otimes |0\rangle\langle 0| + I \otimes |0\rangle\langle 0|$ (refer to Sec. IV A for the quantum gate definitions). In the basis sets, ECR and CZ are two-qubit gates and other gates are one-qubit gates. These two-qubit gates are primitives for constructing CX gate. In our circuit construction, we used CX gates regardless of the target devices. The Qiskit transpiler converts all other gates into the gates in the basis gate set depending on the target devices.

To construct the quantum circuit with the error mitigation methods described in Sec. IV B, we first transpiled the quantum circuits of each Trotter step. The circuit implementation of the Trotter steps is described in Secs. III and IV A. For the transpiling, we used the qubit mapping visualized in Fig. 11. During the transpiling process, the logical qubits are mapped

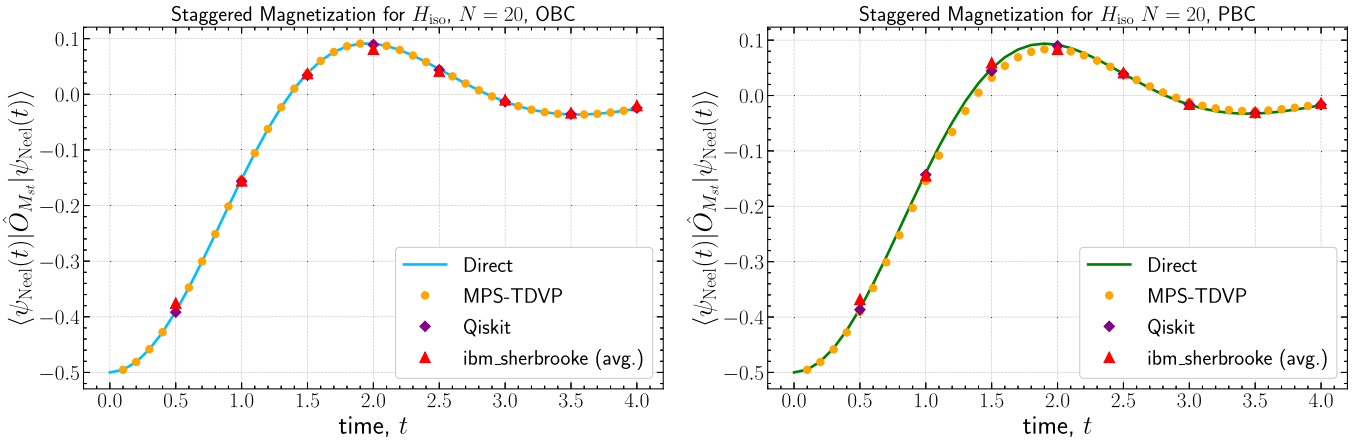

FIG. 7. Time evolution of the expectation value of staggered magnetization for the Néel state under the Hamiltonian $H_{\rm iso}$ for $N = 20$ qubits with OBC (left) and PBC (right), respectively.

to physical qubits as described in Fig. 11, and the logical quantum gates are converted into sets in the basis gate set with circuit optimizations. We applied the highest optimization level during the transpiling.

After that, we duplicated each circuit two times (three circuits including the base circuit) and applied a local unitary gate folding with scaling factors 1, 3, and 5 to the three circuits, respectively. In the next place, we applied the Pauli twirling. We duplicated each circuit 10 times including the base circuit and surrounded the Clifford gate with a randomly chosen Pauli twirling combination out of the prepared Pauli twirling gates set as described in Fig. 6. Finally, we applied the dynamical decoupling method to all those circuits. Up to now, we have thirty circuits for a Trotter step.

To execute each circuit, we used 10 000 shots (repeated circuit execution for the measurement sampling) in all cases. At the end of the circuit executions, we applied the measurement error mitigation method. We used a Python library [61] to calibrate the library from the system error information and to correct the measurement errors. After gathering all the measurement results of ten circuit duplications for the Pauli twirling, the expectation values are computed for each ZNE folding copy (1, 3, and 5 scaling factors). Finally, the ZNE is estimated by a quadratic polynomial fitting curve.

TABLE II. Averaged staggered magnetization with time for $H_{\rm iso}$ and $N = 20$ from five experiments on `ibm_sherbrooke`. The $\pm$ terms represent the standard deviation of the data.

	Staggered magnetization	
Time, t	OBC	PBC
0.5	-0.3752 ± 0.0011	-0.3680 ± 0.0012
1.0	-0.1555 ± 0.0004	-0.1448 ± 0.0007
1.5	0.03741 ± 0.00032	0.591 ± 0.0007
2.0	0.0811 ± 0.0017	0.0836 ± 0.0009
2.5	0.0417 ± 0.0008	0.0413 ± 0.0008
3.0	-0.0099 ± 0.0005	-0.0156 ± 0.0010
3.5	-0.0333 ± 0.0006	-0.0303 ± 0.0007
4.0	-0.0201 ± 0.0008	-0.0137 ± 0.0010

V. RESULTS AND DISCUSSION

To ensure the accuracy of the results obtained from quantum computers, it is crucial to cross-check those results with classical numerical methods used to study the many-body system. Nevertheless, the classical approach becomes inefficient with the number of qubits, given the exponential growth in the dimensionality of the Hilbert space and therefore importance of quantum computing becomes crucial for large-scale calculations. In the following, we briefly present our two adopted classical methods for checking the measured values from IBM's quantum devices.

In the experiments, we limit the initial state to the Néel state in order to focus on the time evolution of the Hamiltonians. Because of the complexity of the implementation of the Hamiltonians and the decoherence limit of the quantum devices, the maximum circuit depth is limited. Therefore, we adopt the Néel state as the initial state (one depth in the implementation regardless of the system size) to minimize the circuit depth for the initial-state preparation.

Direct method. One straightforward approach, denoted the *direct* method in this work, is to calculate the time-evolved expectation value of the staggered magnetization $\hat{O}_{M_{st}}$ for N qubits with respect to the Néel state, $\langle\psi_{\rm Neel}(t)|\hat{O}_{M_{st}}|\psi_{\rm Neel}(t)\rangle$ where $|\psi_{\rm Neel}(t)\rangle = e^{-iHt}|\psi_{\rm Neel}\rangle$. The Hamiltonian H is either the isotropic Hamiltonian $H_{\rm iso}$ or the dimer Hamiltonian $H_{\rm dimer}$ of our study. Here, H is a $2^N \times 2^N$ Hermitian matrix that acts on the Hilbert space of dimension 2^N. We have implemented this approach using our own Python implementation and have checked the results with QuSpin [65]. This method is the simplest and most accurate. However, it becomes an inefficient computational mode for calculating the time evolution of state vectors with $N \gtrsim 20$ qubits, as the Hilbert space's dimensionality increases exponentially with the number of qubits. For example, the number of qubits $N = 50$ requires 16 petabytes of memory allocation in double precision for expressing just a state vector, which is possible only for present supercomputers. Therefore, we turn to the classical approximation method based on matrix product states to calculate the time evolution of state vectors with $N > 20$ qubits.

MPS-TDVP method. Matrix product states (MPSs) is a common method used to study the time evolution of

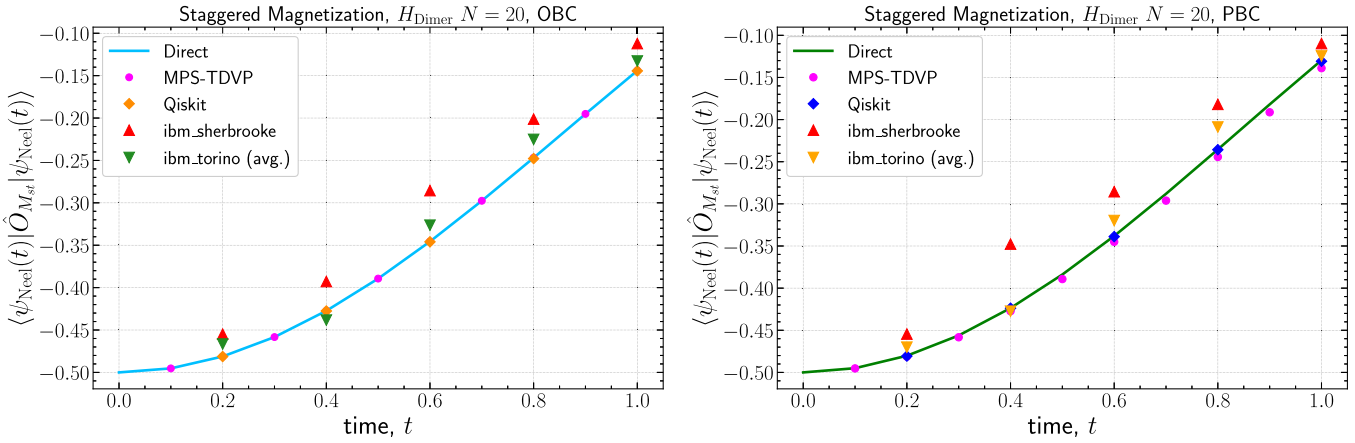

FIG. 8. Time evolution of the expectation value of staggered magnetization with respect to the Néel state under the Hamiltonian H_{dimer} for $N = 20$ qubits.

large quantum many-body systems [66,67]. MPS is a one-dimensional array of tensors linked together, with each tensor corresponding to a site or particle of the many-body system. The indices connecting the tensors in the MPS are called bond indices, which can take up to χ values (also known as bond dimensions). Meanwhile, the open indices of each tensor correspond to the physical degrees of freedom of the local Hilbert space associated with a site or a particle of the system, which can take up to d values (for our system of spin-1/2 particles, $d = 2$). While the MPS can represent any quantum state of the many-body system, the bond dimension χ needs to be exponentially large in the system size to cover all states in the Hilbert space. We determine the time evolution of the expectation value of staggered magnetization for the Néel state, which we denote here as the *MPS-TDVP* method, using approximation method based on time-dependent variational principle (TDVP) [68,69], facilitated by the package ITensor [70–72]. The time evolution of MPS using the TDVP-based method is advantageous as it cannot only handle the Hamiltonian with long-range interactions rather than only the nearest-neighbor interaction but is also computationally less demanding when the PBC is imposed on those Hamiltonians.

In the subsequent analysis, we consider the time parameter t in an arbitrary unit where $\hbar = 1$ and $J_1 = 1$. One can simply restore t in seconds by mapping $t \to \hbar t/J_1$. For a typical value of exchange interaction, $J_1 \sim O(\text{eV})$ that is associated with magnetic materials, t falls in $O(10^{-15})$ s, the timescale of atomic transitions. Besides, we choose $\delta t = 0.1$ as the time-step size and maximum allowed error $\epsilon = 10^{-12}$ for each sweep in the MPS-TDVP method, which leads to 10 and 40 sweeps when we evolve the system up to $t = 1$ and $t = 4$, respectively.

TABLE III. Averaged staggered magnetization with time for H_{dimer} and $N = 20$ from five experiments on `ibm_torino`. The $\pm$ terms represent the standard deviation of the data.

	Staggered magnetization	
Time, t	OBC	PBC
0.2	-0.4665 ± 0.0005	-0.470 ± 0.006
0.4	-0.4383 ± 0.0014	-0.427 ± 0.005
0.6	-0.3264 ± 0.0012	-0.320 ± 0.004
0.8	-0.2252 ± 0.0011	-0.2089 ± 0.0030
1.0	-0.1328 ± 0.0005	-0.1245 ± 0.0014

A. $N = 20$ qubits

We present the time evolution of the expectation value of the staggered magnetization observable for the Néel state under the isotropic Heisenberg Hamiltonian H_{iso} using the second-order Trotterization (Sec. III A) in Fig. 7 for $N = 20$ qubits with OBC and PBC cases, respectively. In the experiments on `ibm_sherbrooke`, we applied the error mitigation techniques which are already delineated in Sec. IV B, and ran each circuit with 100 000 shots (trials). This process was repeated five times. The Qiskit simulation is a Qiskit sampling simulation (`qasm_simulator`) of the circuits with 100 000 shots. The Qiskit experiment is executed once.

From Fig. 7 (left), we can see an excellent agreement among the classical computations (both direct and MPS-TDVP methods), the Qiskit simulation, and the `ibm_sherbrooke` experiments. The plot of `ibm_sherbrooke` is the average of the five executions. We tabulate the average values and the standard deviations in Table II and Appendix A.

TABLE IV. Circuit depth with respect to the Trotter steps for H_{iso} with $N = 20$, 96, 100 qubits after transpiling with the optimization level 3.

	Circuit depth for H_{iso}			
	OBC		PBC	
Trotter step	$N = 20$	$N = 100$	$N = 20$	$N = 96$
1	41	41	40	47
2	67	67	66	77
3	93	93	92	106
4	119	119	118	135
5	145	145	144	164
6	171	171	170	193
7	197	197	196	222
8	223	223	222	251

TABLE V. Number of CX gates for H_{iso} after transpiling with the optimization level 3.

	No. of CX gates for H_{iso}			
	OBC		PBC	
Trotter step	$N = 20$	$N = 100$	$N = 20$	$N = 96$
1	87	447	90	432
2	144	744	150	720
3	201	1041	210	1008
4	258	1338	270	1296
5	315	1635	330	1584
6	372	1932	390	1872
7	429	2229	450	2160
8	486	2526	510	2448

In contrast, in Fig. 7 (right), for PBC, although we also have an excellent agreement among the direct, the Qiskit simulation, and the ibm_sherbrooke experiments, there is a mismatch between the results obtained from the direct and MPS-TDVP methods. This mismatch between the two methods is inherently related to the requirement of a larger bond dimension due to the linking between the tensors at the first and last sites of the many-body system and the resulting larger truncation error compared with the OBC cases. We note that for H_{iso} and $N = 20$ qubits with OBC, the maximum link dimension results in $\chi = 102$ after 40 sweeps as we evolve the system up to $t = 4$. On the other hand, for the PBC case, after 40 sweeps, we end up with $\chi = 991$ while keeping the error within ϵ.

Figure 8 presents the experimental results of $\langle\psi_{\text{Neel}}(t)|\hat{O}_{M_{st}}|\psi_{\text{Neel}}(t)\rangle$ for H_{dimer} with $N = 20$ qubits using the first-order Trotterization (Sec. III B) and comparison with classical computations. The Qiskit simulation is a Qiskit sampling simulation (qasm_simulator) of the circuits with 100 000 shots. The experiments of ibm_sherbrooke and ibm_torino uses 100 000 shots with the QEM (Sec. IV B). The ibm_torino experiment was repeated five times while the ibm_sherbrooke experiment was executed once. The average values and the standard deviations of ibm_torino are tabulated in Table III and Appendix A. The direct computation and the Qiskit simulation show great agreement in both boundary conditions. Again, like the case of H_{iso}, we see a mismatch between the direct computation and the MPS-TDVP for the H_{dimer} with PBC in Fig. 8 (right). In the case of OBC, we get the maximum link dimension to be $\chi = 28$ after 10 sweeps to evolve up to $t = 1$, whereas, for the PBC, it was $\chi = 251$ after 10 sweeps while keeping the error within ϵ. In addition, the ibm_sherbrooke results show a larger discrepancy than the ibm_torino results. We presume the accuracy difference is originated from the hardware accuracy of ibm_torino and ibm_sherbrooke which have 0.8% and 1.7% error per layered gate (EPLG), respectively, in a chain of 100 qubits [73].

In the comparison between the H_{iso} and the H_{dimer}, the ibm_sherbrooke results for H_{iso} in Fig. 7 show a good agreement and the results for H_{dimer} in Fig. 8 have notable discrepancy in both boundary conditions. We conjecture that the reason is that the circuit depth and the number of CX gates are different in each Trotter step as shown in Tables IV, V, VI, VII, and Appendix B. Since the H_{dimer} Hamiltonian has the additional term [refer to Eq. (5)] and the implementation for the additional term needs two layers SWAP gates, the H_{dimer} Hamiltonian implementation needs about 60% more circuit depth than the H_{iso} Hamiltonian implementation.

B. $N = 96$ and $N = 100$ qubits

After cross-checking the measurements of staggered magnetization with the real quantum computers for $N = 20$ qubits with classical (direct and MPS-TDVP) methods and Qiskit simulations, we present here our main results of large-scale quantum simulation of the Heisenberg spin chain. In this extension, we used the same circuit implementation methods, error mitigation methods, and the number of shots (100 000) except for the number of qubits. We used 100 qubits for the OBC. However, since the PBC needs a connection between the first qubit and the last qubit, we adopted 96 qubits for the PBC. The qubit mapping for these cases is depicted in Fig. 11.

In Fig. 9, we can see that the results of $\langle\psi_{\text{Neel}}(t)|\hat{O}_{M_{st}}|\psi_{\text{Neel}}(t)\rangle$ for H_{iso} for $N = 100$ qubits (OBC) with ibm_brisbane (left figure) and $N = 96$ qubits (PBC) with ibm_sherbrooke (right figure), respectively, are in excellent agreement with the results from the MPS-TDVP method. Note that for such large-scale systems with $N \approx 100$

TABLE VI. Circuit depth with respect to the Trotter steps for H_{dimer} with $N = 20$, 96, 100 qubits after transpiling with the optimization level 3.

	Circuit depth for H_{dimer}							
	OBC				PBC			
	$N = 20$		$N = 100$		$N = 20$		$N = 96$	
Trotter step	ibm_sherbrooke	ibm_torino	ibm_brisbane	ibm_torino	ibm_sherbrooke	ibm_torino	ibm_sherbrooke	ibm_torino
1	66	64	71	70	68	64	80	69
2	141	132	155	144	144	132	163	146
3	215	200	239	218	218	200	246	223
4	298	268	293	292	292	268	329	300
5	363	336	407	366	366	336	412	377

TABLE VII. Number of CX gates for H_{dimer} after transpiling with the optimization level 3.

	No. of CX gates for H_{dimer}							
	OBC				PBC			
	$N = 20$		$N = 100$		$N = 20$		$N = 96$	
Trotter step	ibm_sherbrooke	ibm_torino	ibm_brisbane	ibm_torino	ibm_sherbrooke	ibm_torino	ibm_sherbrooke	ibm_torino
1	138	138	738	738	150	150	720	720
2	288	288	1548	1548	315	315	1512	1512
3	438	438	2358	2358	480	480	2304	2304
4	588	588	3168	3168	645	645	3096	3096
5	738	738	3978	3978	810	810	3888	3888

qubits, the direct method and the Qiskit simulations are unavailable.

Figure 10 shows the results of time-evolved staggered magnetization for H_{dimer} with time up to $t = 1$ with $N = 100$ qubits (OBC) (left figure) and $N = 96$ qubits (PBC) (right figure) using ibm_brisbane, ibm_sherbrooke, and ibm_torino. Likewise the $N = 20$ cases, this case shows a notable discrepancy between the results of the IBM quantum devices and the MPS-TDVP results.

As discussed in Sec. V A, we presume that the discrepancy is originated from longer circuit depth and more CX gates in the implementation for the time evolution of H_{dimer}. Also, the difference between ibm_torino and ibm_brisbane is derived from the hardware accuracy of ibm_torino and ibm_brisbane which have 0.8% and 1.9% EPLG, respectively, in a chain of 100 qubits [73].

C. Discussion and future work

The staggered magnetization defined in Eq. (3) represents the antiferromagnetic ordering of spin-1/2 particles on the chain along the z axis, and its value is either 0.5 or -0.5, depending on the chosen ordering. In our specific case, the staggered magnetization of the initial Néel state, as given in Eq. (4), is determined to be -0.5 at $t = 0$. Subsequently, when the system undergoes time evolution driven by either the Isotropic Heisenberg Hamiltonian H_{iso} or the dimer Hamiltonian H_{dimer}, the staggered magnetization of the initial Néel state, which is not an eigenstate of either Hamiltonian, gradually relaxes to zero as time progresses. This behavior is depicted in Figs. 7–10, where the staggered magnetization shifts from its initial value of -0.5 at $t = 0$ towards a value of zero at $t > 0$ during the time evolution.

In Figs. 7 and 9, we tracked the time evolution of the staggered magnetization under H_{iso} up to $t = 4$, demonstrating its relaxation towards zero over time. Conversely, due to limitations posed by larger circuit depths and error rates in real devices, we only determined the time evolution of the staggered magnetization under H_{dimer} up to $t = 1$, as represented by the raised plots in Figs. 8 and 10.

In our experiments, the H_{dimer} cases have larger error rates while all the H_{iso} cases show great accuracy. As the results from the Qiskit simulation also show better consistency with the direct computation at $N = 20$ cases, as seen in Fig. 8, we conclude that the discrepancy comes from the quantum device errors and noises rather than numerical errors of the first-order Trotterization. This also explains the disagreement between the values of quantum devices and the MPS-TDVP method, presented in Fig. 10 for $N = 96$ and $N = 100$ with H_{dimer}. Besides, this conclusion is also supported by the comparison of the results between ibm_torino and ibm_sherbrooke in Fig. 8. The results

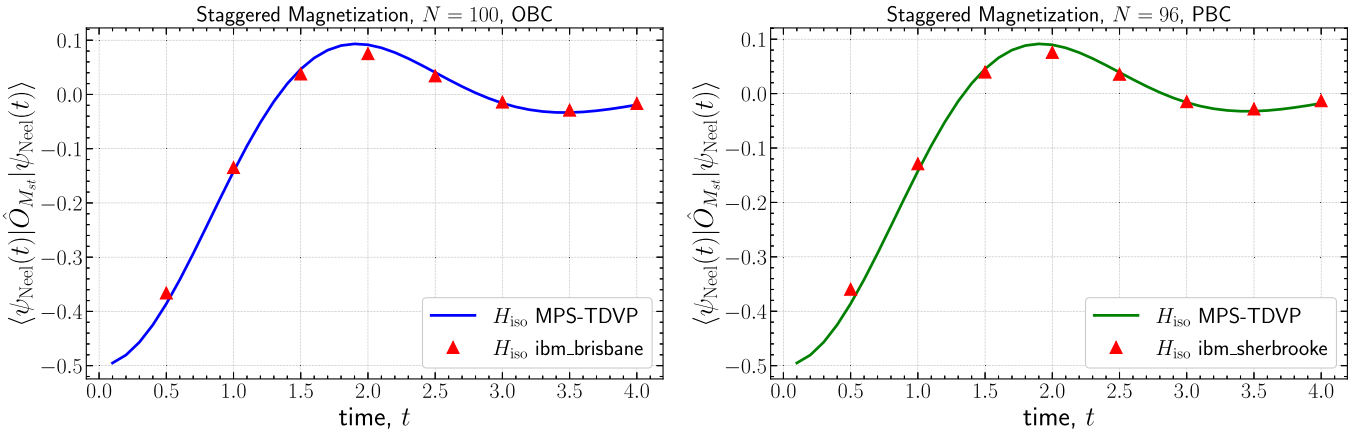

FIG. 9. Time evolution of the expectation value of staggered magnetization for the Néel state under the Hamiltonian H_{iso} for $N = 100$ qubits with OBC and $N = 96$ qubits with PBC.

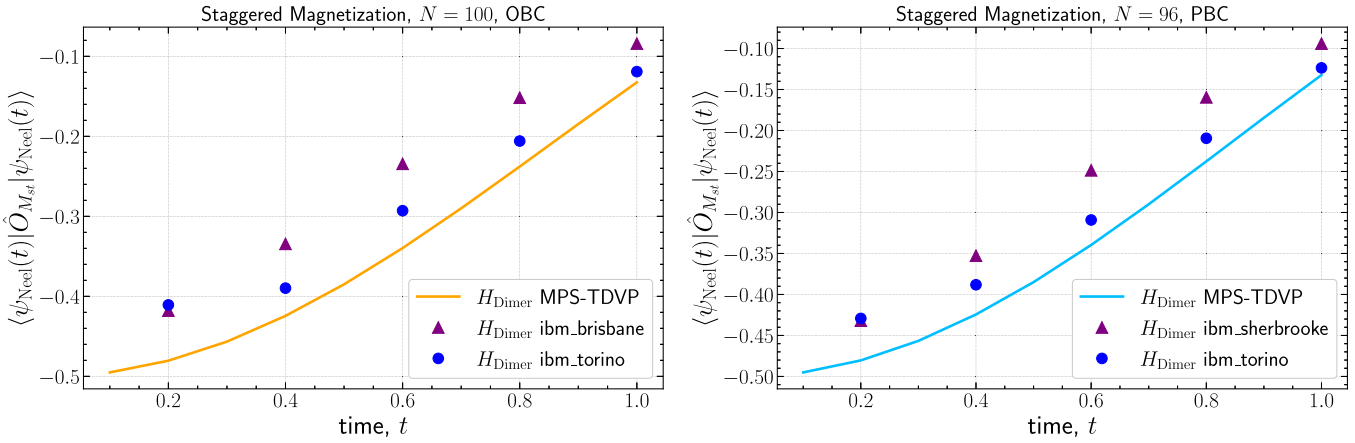

FIG. 10. Time evolution of the expectation value of staggered magnetization for the Néel state under the Hamiltonian H_{dimer} for $N = 100$ qubits with OBC and $N = 96$ qubits with PBC.

of ibm_torino show certainly better accuracy than the results from ibm_brisbane and ibm_sherbrooke because ibm_torino, ibm_sherbrooke, and ibm_sherbrooke have 0.8%, 1.7%, and 1.9% EPLG, respectively, in a chain of 100 qubits [73]. The EPLG measures the average gate process error in a layered chain of 100 qubits. It is derived from a similar quantity known as layer fidelity (LF), and the LF is the process fidelity of the layered chain of 100 qubits [74]. Since the quantum circuit implementation for the H_{dimer} consists of the two parts, J_1 terms and J_2 terms, we conjecture that the main reason for the discrepancy of the H_{dimer} than H_{iso} is a longer circuit depth by the J_2 terms and, in particular, CX gates implementing the SWAP gates of the J_2 terms. The relative errors of the H_{dimer} cases (Figs. 8 and 10) is summarized in Table VIII. The relative errors of each case show the tendency to increase as time evolves. Even though several relative errors decrease as time steps increase, we conjecture the main reason is that the error mitigation methods applied to our experiments work nonlinearly with respect to the circuit depth.

Even though our experiments adopt specific numbers for the parameters, J_1 and J_2, in Eq. (1), the methods applied to the experiments can be easily extended to any number of J_1, J_2 because they change the angles of R_z gates in Eq. (8) and does not change the structure of the quantum circuit such as the circuit depth and the number of CX gates. When we have $\Delta \neq 1$, the optimized circuit implementation of Eq. (8) is impossible. However, it can be implemented by using different angles in Eq. (7) even though the circuit implementation is noisier than Eq. (8) because of more CX gates. Hence, a more efficient circuit implementation for the case of $\Delta \neq 1$ will be our future work.

In our future work, we study how to fine-tune the parameters of the error mitigation methods discussed in Sec. IV B. In particular, we assume that there will be a better extrapolation fitting function for the H_{dimer} cases. Additionally, we explore other quantum error mitigation methods and find ways to combine them more efficiently. Furthermore, we plan to extend our study to include valid state preparation before the time evolution, allowing us to tackle more realistic quantum simulation problems.

VI. CONCLUSION AND OUTLOOK

In conclusion, our study represents a significant step forward in the realm of quantum simulation before the fault tolerance quantum era, as we successfully implemented the quantum simulation of a frustrated quantum spin-$\frac{1}{2}$ antiferromagnetic Heisenberg spin chain on IBM's superconducting quantum computer. The incorporation of both nearest-neighbor J_1 and next-nearest-neighbor J_2 exchange interactions, particularly utilizing first-order Trotterization

TABLE VIII. Relative error (%) in the measured value of the staggered magnetization with time for H_{dimer} with $N = 20, 96, 100$ qubits.

	Relative error (%) in measured staggered magnetization							
	OBC				PBC			
	$N = 20$		$N = 100$		$N = 20$		$N = 96$	
Time	ibm_sherbrooke	ibm_torino(avg.)	ibm_brisbane	ibm_torino	ibm_sherbrooke	ibm_torino(avg.)	ibm_sherbrooke	ibm_torino
0.2	5.47%	3.05%	13.04%	14.51%	5.37%	2.12%	10.10%	10.66%
0.4	8.08%	2.56%	21.21%	8.17%	18%	0.88%	17%	8.54%
0.6	17.38%	5.57%	31.01%	13.75%	15.55%	5.42%	26.80%	9%
0.8	18.50%	8.80%	36.20%	13.41%	22.74%	11.30%	32.86%	11.85%
1.0	22.17%	7.87%	36.57%	10.10%	15.26%	3.90%	29%	6.57%

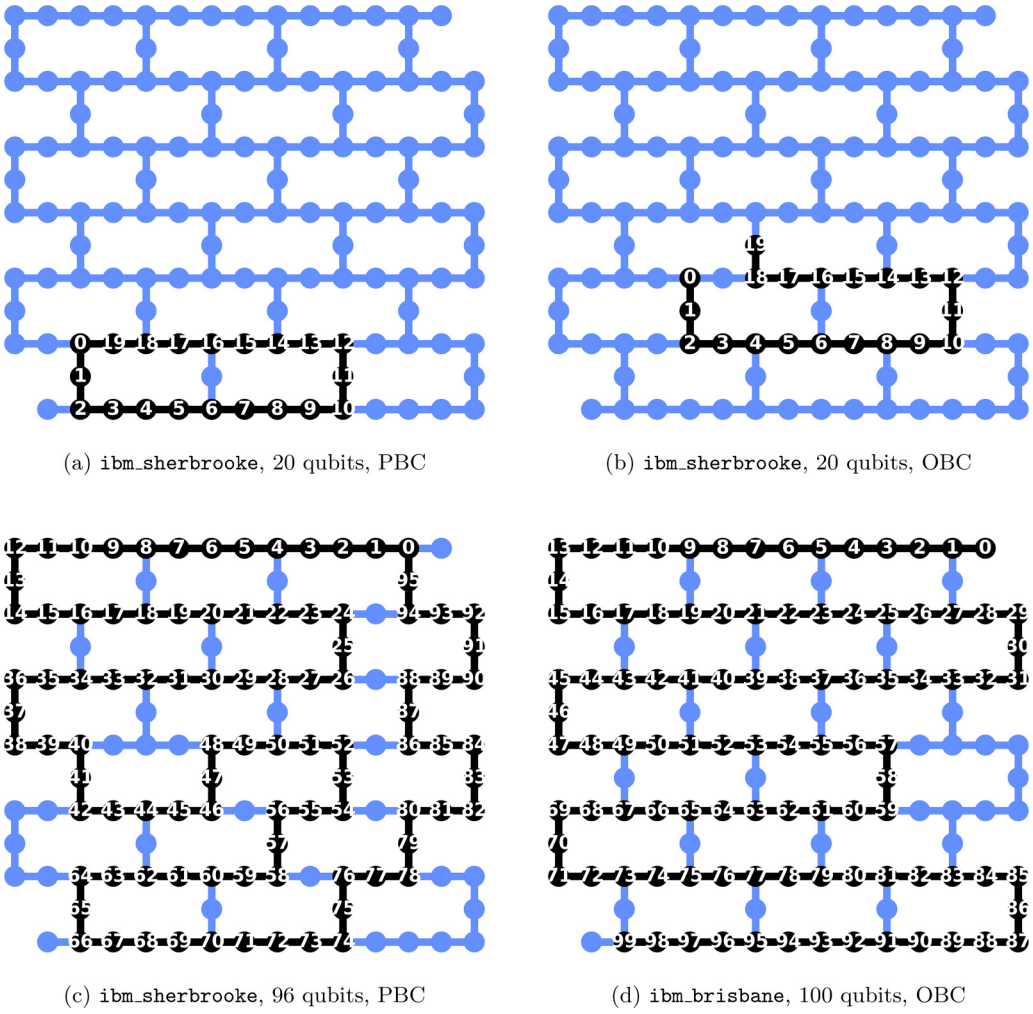

(a) ibm_sherbrooke, 20 qubits, PBC

(b) ibm_sherbrooke, 20 qubits, OBC

(c) ibm_sherbrooke, 96 qubits, PBC

(d) ibm_brisbane, 100 qubits, OBC

FIG. 11. Circuit qubit mapping layout.

for the latter, demonstrates the versatility and capability of quantum computing technologies. Notably, our application of second-order Trotterization for the isotropic Heisenberg spin chain, coupled with precise measurements of staggered magnetization expectation values across a substantial range of qubits (up to 100), establishes the potential of these quantum devices for investigating properties of large-scale quantum systems.

The constant circuit depth achieved in each Trotter step, independent of the initial qubit number, adds a practical dimension to our findings, addressing a critical aspect of quantum simulation scalability. Moreover, our ability to accurately measure expectation values for such a large-scale quantum system using superconducting quantum computers underscores their utility in probing the intricacies of many-body quantum systems.

In this study, we broaden the applicability of noisy quantum computers to encompass more intricate scenarios involving the time dynamics of Hamiltonians on a larger scale, specifically within the context of noisy superconducting quantum computers. In the future, our efforts pave the way for forthcoming quantum computing calculations, showcasing the quantum advantage over classical methods in simulating intricate quantum systems more prominently. As we continue to push the boundaries of quantum computing capabilities, our findings contribute to the growing body of evidence supporting the transformative potential of quantum computers in advancing our understanding of quantum phenomena.

ACKNOWLEDGMENTS

We thank Taku Izubuchi, Kyoungchul Kong, and John Ralston for useful discussions and communications. This work is supported by the U.S. Department of Energy, Office of Science, Grant No. DE-SC0012704 (K.Y. and R.S.S.), the Special Postdoctoral Researchers Program of RIKEN and RIKEN-BNL Research Center (R.S.S.), and the Brookhaven National Laboratory LDRD #24-061 (K.Y.). This research used quantum computing resources of the Oak Ridge Leadership Computing Facility, which is a DOE Office of Science User Facility supported under Contract DE-AC05-00OR22725. This research used resources of the National Energy Research Scientific Computing Center, a DOE Office of Science User Facility supported by the Office of Science of the U.S. Department of Energy under Contract No.

DE-AC02-05CH11231 using NERSC award NERSC DDR-ERCAP0024165 and DDR-ERCAP0028999.

APPENDIX A: AVERAGED STAGGERED MAGNETIZATION FOR $N = 20$

In this Appendix, we present the averaged value of the staggered magnetization with respect to the Néel state for simulation time in the case of isotropic Heisenberg Hamiltonian H_{iso} and the dimer Hamiltonian H_{dimer} presented in Figs. 7 and 8. For the case of H_{iso} with $N = 20$ qubits, we perform five repeated experiments of the staggered magnetization on `ibm_sherbrooke` for both OBC and PBC, and obtain the corresponding averaged value in each Trotter time steps up to $t = 4$. The following term of $\pm$ represents the standard deviation of the data.

In addition, for H_{dimer} with $N = 20$ qubits, we use `ibm_torino` to measure the staggered magnetization repeatedly five times at each Trotter time step up to $t = 1$, and determine the average value. The standard deviations in Tables II and III show that each experimental datum is distributed close to the average value.

APPENDIX B: CIRCUIT DEPTH AND CX GATE COUNTS

We present the circuit depth and `CX` gate counts for Trotter steps associated with the Trotterization circuits for the Hamiltonians H_{iso} and H_{dimer}, respectively. The circuit depth is an important measure of how many operations one can implement before the coherence breaks down in a quantum computer. Therefore, the circuit depth associated with the Trotterization circuits essentially captures how reliable the time evolutions of spin-chain under the isotropic Heisenberg and the dimer Hamiltonians are, and how the system size scales with the initial number of qubits. In addition, `CX` is the noisiest gate in the base gate set. Hence, measuring the number of `CX` gates in a circuit can be used to estimate the noise of the circuit. In the following tables, the circuit depths and the number of `CX` gates are measured transpiling with the optimization level 3 in Qiskit. Refer to Tables IV, V, VI, and VII.

APPENDIX C: RELATIVE ERROR IN MEASURED STAGGERED MAGNETIZATION FOR H_{dimer}

In this section, we tabulate the relative error in measured value of the staggered magnetization with respect to its theoretical value for different simulation time when evolving under the dimer Hamiltonian. The relative error in percentage is given by

$$\delta x = \left| \frac{x_0 - x}{x} \right| \times 100\%, \tag{C1}$$

where x and x_0 are the theoretical and measured value of the staggered magnetization, respectively. For $N = 20$ with both OBC and PBC cases, we use theoretical values from *direct* method as they are the most exact values. On the other hand, for $N = 96$ (PBC) and $N = 100$ (OBC) cases, we only have approximate theoretical values from *MPS-TDVP* method. Refer to Table VIII,

APPENDIX D: CIRCUITE QUBIT MAPPING LAYOUT

Here, we present the qubit mappings of `ibm_sherbrooke` and `ibm_brisbane` for $N = 20$, 96, and 100 qubits in Fig. 11 which are used in our experiments. Refer to Fig. 11.

[1] J. Preskill, Quantum computing in the NISQ era and beyond, Quantum **2**, 79 (2018).

[2] K. Bharti, A. Cervera-Lierta, T. H. Kyaw, T. Haug, S. Alperin-Lea, A. Anand, M. Degroote, H. Heimonen, J. S. Kottmann, T. Menke, W.-K. Mok, S. Sim, L.-C. Kwek, and A. Aspuru-Guzik, Noisy intermediate-scale quantum algorithms, Rev. Mod. Phys. **94**, 015004 (2022).

[3] J. I. Cirac and P. Zoller, Goals and opportunities in quantum simulation, Nat. Phys. **8**, 264 (2012).

[4] I. M. Georgescu, S. Ashhab, and F. Nori, Quantum simulation, Rev. Mod. Phys. **86**, 153 (2014).

[5] A. J. Daley, I. Bloch, C. Kokail, S. Flannigan, N. Pearson, M. Troyer, and P. Zoller, Practical quantum advantage in quantum simulation, Nature (London) **607**, 667 (2022).

[6] S. Lloyd, Universal quantum simulators, Science **273**, 1073 (1996).

[7] D. S. Abrams and S. Lloyd, Simulation of many-body Fermi systems on a universal quantum computer, Phys. Rev. Lett. **79**, 2586 (1997).

[8] S. Somaroo, C. H. Tseng, T. F. Havel, R. Laflamme, and D. G. Cory, Quantum simulations on a quantum computer, Phys. Rev. Lett. **82**, 5381 (1999).

[9] C. Zalka, Simulating quantum systems on a quantum computer, Proc. R. Soc. London, Ser. A **454**, 313 (1998).

[10] E. Farhi, J. Goldstone, S. Gutmann, and M. Sipser, Quantum computation by adiabatic evolution, arXiv:quant-ph/0001106.

[11] G. Ortiz, J. E. Gubernatis, E. Knill, and R. Laflamme, Quantum algorithms for fermionic simulations, Phys. Rev. A **64**, 022319 (2001).

[12] R. Somma, G. Ortiz, J. E. Gubernatis, E. Knill, and R. Laflamme, Simulating physical phenomena by quantum networks, Phys. Rev. A **65**, 042323 (2002).

[13] D. W. Berry, G. Ahokas, R. Cleve, and B. C. Sanders, Efficient quantum algorithms for simulating sparse Hamiltonians, Commun. Math. Phys. **270**, 359 (2007).

[14] A. M. Childs and R. Kothari, Simulating sparse Hamiltonians with star decompositions, *Lecture Notes in Computer Science* (Springer, Berlin, Heidelberg, 2011), Vol. 6519, p. 94.

[15] S. Endo, S. C. Benjamin, and Y. Li, Practical quantum error mitigation for near-future applications, Phys. Rev. X **8**, 031027 (2018).

[16] K. Temme, S. Bravyi, and J. M. Gambetta, Error mitigation for short-depth quantum circuits, Phys. Rev. Lett. **119**, 180509 (2017).

[17] Y. Li and S. C. Benjamin, Efficient variational quantum simulator incorporating active error minimisation, Phys. Rev. X **7**, 021050 (2017).

[18] A. Kandala, K. Temme, A. D. Córcoles, A. Mezzacapo, J. M. Chow, and J. M. Gambetta, Error mitigation extends the computational reach of a noisy quantum processor, Nature (London) **567**, 491 (2019).

[19] E. van den Berg, Z. K. Minev, A. Kandala, and K. Temme, Probabilistic error cancellation with sparse Pauli-Lindblad models on noisy quantum processors, Nat. Phys. **19**, 1116 (2023).

[20] H. Yu, Y. Zhao, and T.-C. Wei, Simulating large-size quantum spin chains on cloud-based superconducting quantum computers, Phys. Rev. Res. **5**, 013183 (2023).

[21] Y. Kim, C. J. Wood, T. J. Yoder, S. T. Merkel, J. M. Gambetta, K. Temme, and A. Kandala, Scalable error mitigation for noisy quantum circuits produces competitive expectation values, Nat. Phys. **19**, 752 (2023).

[22] Y. Kim, A. Eddins, S. Anand, K. X. Wei, E. van den Berg, S. Rosenblatt, H. Nayfeh, Y. Wu, M. Zaletel, K. Temme, and A. Kandala, Evidence for the utility of quantum computing before fault tolerance, Nature (London) **618**, 500 (2023).

[23] P. Fazekas and P. W. Anderson, On the ground state properties of the anisotropic triangular antiferromagnet, Philos. Mag. **30**, 423 (1974).

[24] B. Sriram Shastry and B. Sutherland, Exact ground state of a quantum mechanical antiferromagnet, Physica B + C (Amsterdam) **108**, 1069 (1981).

[25] L. Balents, Spin liquids in frustrated magnets, Nature (London) **464**, 199 (2010).

[26] F. D. M. Haldane, Spontaneous dimerization in the $s = \frac{1}{2}$ Heisenberg antiferromagnetic chain with competing interactions, Phys. Rev. B **25**, 4925 (1982).

[27] F. D. M. Haldane, Erratum: Spontaneous dimerization in the $s = \frac{1}{2}$ Heisenberg antiferromagnetic chain with competing interactions, Phys. Rev. B **26**, 5257(E) (1982).

[28] K. Okamoto and K. Nomura, Fluid-dimer critical point in $s = 12$ antiferromagnetic Heisenberg chain with next nearest neighbor interactions, Phys. Lett. A **169**, 433 (1992).

[29] K. Nomura and K. Okamoto, Critical properties of $s = 1/2$ antiferromagnetic XXZ chain with next-nearest-neighbour interactions, J. Phys. A: Math. Gen. **27**, 5773 (1994).

[30] S. R. White and I. Affleck, Dimerization and incommensurate spiral spin correlations in the zigzag spin chain: Analogies to the Kondo lattice, Phys. Rev. B **54**, 9862 (1996).

[31] S. Eggert, Numerical evidence for multiplicative logarithmic corrections from marginal operators, Phys. Rev. B **54**, R9612 (1996).

[32] C. Mudry, A. Furusaki, T. Morimoto, and T. Hikihara, Quantum phase transitions beyond Landau-Ginzburg theory in one-dimensional space revisited, Phys. Rev. B **99**, 205153 (2019).

[33] P. Wiegmann, Topological superconductivity, Prog. Theor. Phys. Suppl. **107**, 243 (1992).

[34] M. C. Diamantini, P. Sodano, E. Langmann, and G. W. Semenoff, SU(N) antiferromagnets and the phase structure of QED in the strong coupling limit, Nucl. Phys. B **406**, 595 (1993).

[35] Y. Hosotani, Gauge theory model: Quark dynamics and antiferromagnets, arXiv:hep-th/9606167.

[36] Y. Hosotani, Gauge theory description of spin ladders, J. Phys. A: Math. Gen. **30**, L757 (1997); **31**, 7415 (1998).

[37] H. F. Trotter, On the product of semi-groups of operators, Proc. Am. Math. Soc. **10**, 545 (1959).

[38] M. Suzuki, Generalized Trotter's formula and systematic approximants of exponential operators and inner derivations with applications to many-body problems, Commun. Math. Phys. **51**, 183 (1976).

[39] M. Suzuki, On the convergence of exponential operators-the Zassenhaus formula, BCH formula and systematic approximants, Commun. Math. Phys. **57**, 193 (1977).

[40] C. K. Majumdar and D. K. Ghosh, On next-nearest-neighbor interaction in linear chain. I, J. Math. Phys. **10**, 1388 (1969).

[41] C. K. Majumdar, Antiferromagnetic model with known ground state, J. Phys. C: Solid State Phys. **3**, 911 (1970).

[42] M. Vanicat, L. Zadnik, and T. Prosen, Integrable Trotterization: Local conservation laws and boundary driving, Phys. Rev. Lett. **121**, 030606 (2018).

[43] A. Smith, M. S. Kim, F. Pollmann, and J. Knolle, Simulating quantum many-body dynamics on a current digital quantum computer, npj Quantum Inf. **5**, 106 (2019).

[44] K. Zhang, K. Yu, K. Hao, and V. Korepin, Optimal realization of Yang–Baxter gate on quantum computers, Adv. Quantum Technol. **7**, 2300345 (2024).

[45] P. W. Shor, Scheme for reducing decoherence in quantum computer memory, Phys. Rev. A **52**, R2493 (1995).

[46] A. R. Calderbank and P. W. Shor, Good quantum error-correcting codes exist, Phys. Rev. A **54**, 1098 (1996).

[47] I. D. Kivlichan, C. Gidney, D. W. Berry, N. Wiebe, J. McClean, W. Sun, Z. Jiang, N. Rubin, A. Fowler, A. Aspuru-Guzik, H. Neven, and R. Babbush, Improved fault-tolerant quantum simulation of condensed-phase correlated electrons via Trotterization, Quantum **4**, 296 (2020).

[48] J. Lee, D. W. Berry, C. Gidney, W. J. Huggins, J. R. McClean, N. Wiebe, and R. Babbush, Even more efficient quantum computations of chemistry through tensor hypercontraction, PRX Quantum **2**, 030305 (2021).

[49] C. Charles, E. J. Gustafson, E. Hardt, F. Herren, N. Hogan, H. Lamm, S. Starecheski, R. S. Van de Water, and M. L. Wagman, Simulating $\mathbb{Z}_2$ lattice gauge theory on a quantum computer, arXiv:2305.02361.

[50] T. Giurgica-Tiron, Y. Hindy, R. LaRose, A. Mari, and W. J. Zeng, Digital zero noise extrapolation for quantum error mitigation, *2020 IEEE International Conference on Quantum Computing and Engineering (QCE)* (IEEE, Denver, CO, USA, 2020), pp. 306–316.

[51] C. H. Bennett, G. Brassard, S. Popescu, B. Schumacher, J. A. Smolin, and W. K. Wootters, Purification of noisy entanglement and faithful teleportation via noisy channels, Phys. Rev. Lett. **76**, 722 (1996).

[52] J. J. Wallman and J. Emerson, Noise tailoring for scalable quantum computation via randomized compiling, Phys. Rev. A **94**, 052325 (2016).

[53] Z. Cai and S. C. Benjamin, Constructing smaller Pauli twirling sets for arbitrary error channels, Sci. Rep. **9**, 11281 (2019).

[54] L. Viola, E. Knill, and S. Lloyd, Dynamical decoupling of open quantum systems, Phys. Rev. Lett. **82**, 2417 (1999).

[55] N. Ezzell, B. Pokharel, L. Tewala, G. Quiroz, and D. A. Lidar, Dynamical decoupling for superconducting qubits: A performance survey, Phys. Rev. Appl. **20**, 064027 (2023).

[56] S. Niu and A. Todri-Sanial, Effects of dynamical decoupling and pulse-level optimizations on IBM quantum computers, IEEE Trans. Quantum Eng. **3**, 1 (2022).

[57] S. Bravyi, S. Sheldon, A. Kandala, D. C. Mckay, and J. M. Gambetta, Mitigating measurement errors in multiqubit experiments, Phys. Rev. A **103**, 042605 (2021).

[58] M. R. Geller, Rigorous measurement error correction, Quantum Sci. Technol. **5**, 03LT01 (2020).

[59] K. E. Hamilton, T. Kharazi, T. Morris, A. J. McCaskey, R. S. Bennink, and R. C. Pooser, Scalable quantum processor noise characterization, arXiv:2006.01805.

[60] P. D. Nation, H. Kang, N. Sundaresan, and J. M. Gambetta, Scalable mitigation of measurement errors on quantum computers, PRX Quantum **2**, 040326 (2021).

[61] M3 library, https://github.com/qiskit-extensions/mthree (2023).

[62] J. M. Chow, A. D. Córcoles, J. M. Gambetta, C. Rigetti, B. R. Johnson, J. A. Smolin, J. R. Rozen, G. A. Keefe, M. B. Rothwell, M. B. Ketchen, and M. Steffen, Simple all-microwave entangling gate for fixed-frequency superconducting qubits, Phys. Rev. Lett. **107**, 080502 (2011).

[63] A. D. Córcoles, E. Magesan, S. J. Srinivasan, A. W. Cross, M. Steffen, J. M. Gambetta, and J. M. Chow, Demonstration of a quantum error detection code using a square lattice of four superconducting qubits, Nat. Commun. **6**, 6979 (2015).

[64] Ibmq ecr gate, https://docs.quantum.ibm.com/api/qiskit/qiskit.circuit.library.ECRGate.

[65] P. Weinberg and M. Bukov, QuSpin: A Python package for dynamics and exact diagonalisation of quantum many body systems part I: Spin chains, SciPost Phys. **2**, 003 (2017).

[66] S. Paeckel, T. Köhler, A. Swoboda, S. R. Manmana, U. Schollwöck, and C. Hubig, Time-evolution methods for matrix-product states, Ann. Phys. (NY) **411**, 167998 (2019).

[67] J. I. Cirac, D. Perez-Garcia, N. Schuch, and F. Verstraete, Matrix product states and projected entangled pair states: Concepts, symmetries, theorems, Rev. Mod. Phys. **93**, 045003 (2021).

[68] J. Haegeman, J. I. Cirac, T. J. Osborne, I. Pižorn, H. Verschelde, and F. Verstraete, Time-dependent variational principle for quantum lattices, Phys. Rev. Lett. **107**, 070601 (2011).

[69] J. Haegeman, C. Lubich, I. Oseledets, B. Vandereycken, and F. Verstraete, Unifying time evolution and optimization with matrix product states, Phys. Rev. B **94**, 165116 (2016).

[70] M. Fishman, S. R. White, and E. M. Stoudenmire, The ITensor software library for tensor network calculations, SciPost Phys. Codebases 4 (2022).

[71] M. Fishman, S. R. White, and E. M. Stoudenmire, Codebase release 0.3 for ITensor, SciPost Phys. Codebases, 4 (2022).

[72] https://github.com/ITensor/ITensorTDVP.jl.git.

[73] IBM Quantum system information, https://docs.quantum.ibm.com/run/system-information (2023).

[74] D. C. McKay, I. Hincks, E. J. Pritchett, M. Carroll, L. C. G. Govia, and S. T. Merkel, Benchmarking quantum processor performance at scale, arXiv:2311.05933.